Subcritical Pipe Flow Transition Control Using Dielectric Barrier Discharge Plasma Actuators

Iliya Romm, David Greenblatt and Mark Ishay
Faculty of Mechanical Engineering, Technion – Israel Institute of Technology

Abstract
This work details the application of dielectric barrier discharge (DBD) actuators to the control of transition in subcritical Reynolds number ($250 \leq Re \leq 1000$) circular pipe flows for the purposes of increasing mixing or momentum and heat transfer. Primary flow measurements were made using a single hot-wire anemometer and these were augmented using smoke filament visualization with high-speed photography. A sensitive balance was used to calibrate the body force generated by the actuator as a function of input power. Several distinct actuator configurations were considered and a down-selection indicated that the introduction of swirl produced the largest coherent oscillations and purely turbulent fluctuations. Using the swirl actuator, a detailed parametric study was conducted where operation parameters such as duty cycle, input power, frequency, momentum, etc. were systematically varied. The largest coherent oscillations occurred at a reduced frequency of approximately 0.08 while peak non-coherent disturbances occurred around 0.34. High-speed flow visualization indicated a complex three-dimensional flow structure within the actuated flow regime, with regions of localized reverse flow or vortex breakdown. Several diameters downstream, however, the flow became essentially axi-symmetric in a phase-averaged sense and a fairly simple theoretical model could be used to describe the basic flow mechanisms.

1. INTRODUCTION

Laminar flows are often desirable because the friction losses are less than those in turbulent flows. However, in other instances turbulence is desirable because it produces increases in momentum transfer, fluid mixing, chemical reactions and heat transfer. In many instances, laminar flows will not undergo natural transition to turbulence. It is considered that for small Reynolds numbers, usually referred to as subcritical Reynolds numbers: $Re < Re_c$, the damping effect due to the insufficiently large inertial forces relative to the viscous ones is strong enough to ensure that small perturbations are suppressed (Schlichting and Gersten, 1999). For example, in low Reynolds number air flows over wings where the boundary layer does not undergo transition, the flow may separate prematurely from the wing surface leading to loss of lift and increased drag (Carmichael, 1981). This can be overcome by passively "tripping" the boundary layer (Wieselsberger, 1914; Goldstein, 1936; Reshotko and Tumin, 2004), actively exciting instabilities via very small disturbances (Schubauer and Skramstad, 1943), or actively forcing the flow with large amplitude perturbations. The latter two methods are generally known as active flow control. When Reynolds numbers are well below critical, generally some form of high amplitude active flow control is required to force the flow (e.g. Greenblatt *et al*, 2008).

In circular pipe flows, it is well known that turbulent flows cannot be sustained at Reynolds numbers below approximately 2,000. It is not clear what the critical Reynolds number is with quoted values ranging between 1760 and 2300 (Kerswell, 2005). This Reynolds number range is typical for transition studies, where the phenomenon is often referred to as "bypass transition" (see Morkovin & Reshotko 1990; Morkovin 1993; Reshotko, 1994). This is because the parabolic velocity profile is linearly stable hence transition "bypasses" the stage of Tollmien-Schlichting (TS) waves that are observed in boundary layer flows. The perturbation of pipe flows has historically been used as a means to study transition. Leite (1959) introduced axially symmetric disturbances of large amplitude into a fully developed pipe flow by oscillating a thin sleeve adjacent to the pipe wall. He observed that transition to turbulence occurs when the disturbance amplitude exceeds a "threshold value" which decreases with increasing Reynolds number for $Re \geq 6{,}600$. Fox *et al*. (1968) excited a pipe flow with two helical modes having indices $m = \pm 1$ and constructed a "neutral curve" in frequency-Reynolds space for $Re \geq 2{,}000$. Eliyahou *et al*. (1998)

introduced simultaneous excitation of the azimuthal periodic modes m = + 2 and m = –2 at *Re*~2,200. At small amplitudes the disturbances decayed in the direction of streaming; at intermediate amplitudes they initially amplified and then decayed; and at higher amplitudes transition occurred. This work was extended by Han *et al*. (2000) and it was concluded that the late stages of transition in a pipe flow and in a boundary layer are similar. Investigations at similar Reynolds numbers were conducted by a number of groups, e.g. Darbyshire & Mullin (1995), Draad *et al*. (1998).

When perturbations are introduced into a laminar pipe flow at $Re < Re_c$, they will always decay downstream, irrespective of their original amplitude. In particular, for passive perturbations that are geometrically small compared to the pipe diameter, their associated Reynolds numbers are typically <100 and hence these disturbances decay rapidly downstream. This imposes practical limits on the momentum transfer and mixing at these low Reynolds numbers. If large active perturbations and invoked to force the flow, local transition to turbulence can be achieved, leading to enhanced momentum transfer and mixing over some extent of the pipe length. In this work dielectric barrier discharge (DBD) plasma actuators were chosen to introduce pulsed perturbations into the flow. DBD's are known to be used in aerodynamic applications to control airflows (Moreau, 2007) due to their ability to introduce momentum in a wall-jet-like form (Post and Corke, 2004). While accepting that the turbulence will ultimately decay downstream, active control applied judiciously holds potential for localized increases in overall momentum and mixing. With this in mind, the global objective of this research is to generate and locally sustain turbulence in pipe flows at subcritical Reynolds numbers, using DBD plasma actuators. Generating high turbulence levels and reducing the downstream decay rate are clearly major objectives. Associated with this, is the objective of reducing the input power, or momentum, required to achieve a prescribed turbulence increase. Turbulence generated in these flows would benefit any industrial processes where increases momentum transfer, mixing, chemical reactions and heat transfer are desirable.

2. EXPERIMENTAL METHODS

2.1 The Pipe-Flow Setup

Experiments were performed in an air-based pipe-flow facility, incorporating a segmented glass pipe with a nominal diameter of $D = 2R = 25.4$mm. Adjacent glass pipe segments were joined with Teflon sleeves. A bell-mouth entrance contraction was housed within a large plenum. The plenum was supplied with regulated, filtered and monitored air flow at the opposite end. A baffle plate and multiple fine screens were used to reduce the disturbances in the plenum upstream of the pipe flow bell-mouth (see fig. 1). The subcritical Reynolds number range $250 \leq Re \leq 1{,}000$ was considered where $Re \equiv \rho U_b D/\mu$, U_b being the bulk (mean) flow velocity. Different pipe-lengths were obtained by adding or removing pipe length segments. Variable-height supports were placed beneath the Teflon sleeves in order to maintain a stable and horizontal pipe setup. All flowfield measurements were made within the pipe using a constant temperature single-component hot-wire anemometer. The anemometer used was an AN-1003® (AA Lab Systems) which, according to the manufacturer's specification, has a velocity measurement accuracy of 0.005% and a 1.2 μsec response time.

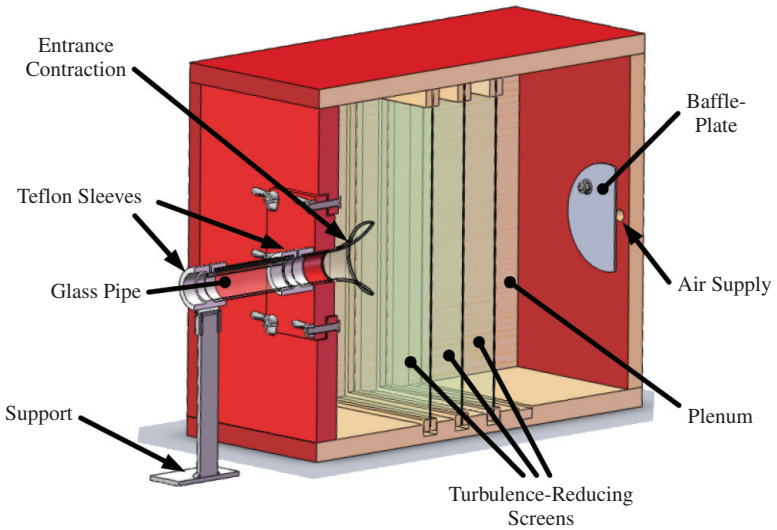

Figure 1. Cutaway schematic of the experimental facility. Plasma actuators are not shown.

The DBD actuator configurations employed here were based on the well known asymmetric configuration consisting of two thin metal electrodes (each 50 μm thick) separated by a dielectric layer (e.g. Roth, 1998; Corke *et al.,* 2004). High Oscillatory voltages, typically at f_{ion} = 20kHz, supplied to the actuators, cause the air to weakly ionize at the edges of the exposed electrodes. These are regions of high electric field potential. When these actuators are deployed in an asymmetric configuration, such as those shown in figs. 2a and 2b, the plasma generated moves to regions of increasing electric field gradients, where the charged ions collide with neutrally charged molecules. For the configurations shown in figs. 2a and 2b, this induces a wall jet to the left along the surface of the dielectric, thereby adding momentum that can be exploited for active flow control.

Actuators were attached to the pipe at z/D = 3.7 (downstream of the pipe entrance) in either an axisymmetric configuration as shown in fig. 2a or a swirl configuration shown in fig. 2b. The glass pipe served the function of the dielectric material between the electrodes, where the outer one was encapsulated using dielectric tape (see fig. 2). In the axisymmetric configuration shown in fig. 2a, an axisymmetric wall-jet was produced, directed either upstream (AU) as shown in the figure or downstream (AD). Changing between the AU and AD configurations merely entailed changing the direction of the pipe segment containing the actuator. For the swirl configuration (S) the actuator was attached longitudinally along the pipe wall (in the axial z-direction); this configuration produced an azimuthal wall-jet as shown in fig. 2b. When the AD and AU actuators were employed, the intention was to generate turbulence by means of a local inflectional (Kelvin-Helmholtz) instability; in the S actuator case, the intention was to generate turbulence via the mechanism of local vortex breakdown. A cylindrical coordinate system $\mathbf{x} = (r,\theta,z)$ was adopted, corresponding to the radial, azimuthal and axial directions respectively, with corresponding velocity components $\mathbf{v} = (u_r, u_\theta, u)$.[1]

For both the axisymmetric and swirl configurations the length of the actuators was the same, namely πD. Gross oscillatory disturbances were produced by pulsing the actuator at a wide range of frequencies (f), amplitudes (expressed as plasma body force, F_p) and pulse-widths (T_{on}). The force developed was calibrated independently using a lever and balance setup similar to that of Enloe *et al.* (2004). All hot-wire measurements were made downstream of the actuator ($L > 0$) as shown in fig. 2a.

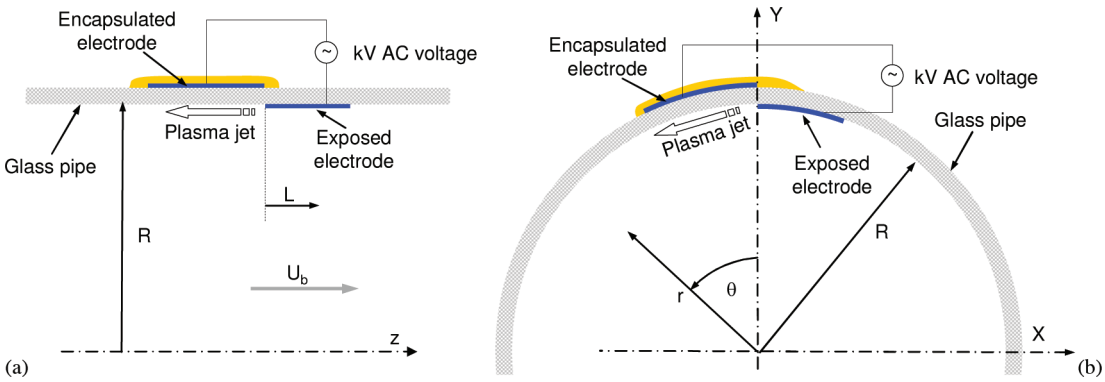

Figure 2. Schematics of the actuator configurations used: (a) axisymmetric upstream oriented (AU); changing the orientation produced axisymmetric downstream oriented (AD) actuation; (b) swirl-type (S) based actuation.

Velocity field measurements within the pipe were made using a single component hotwire anemometer. Profile measurements at L/D = 21.7, with the swirl actuator present upstream but in the absence of control actuation, revealed nearly parabolic velocity profiles at all Reynolds numbers considered. The largest deviation was at Re = 1,000, where the flow was not yet fully developed. The relatively small deviations from the theory were assumed to be due to the presence of the actuator's electrode and associated soldered joints within the pipe upstream of the measurement location. The unsteadiness or "turbulence" level associated with the laminar profiles was negligibly small, never exceeding 2% near the wall and 0.5% at the pipe centerline.

[1]The subscript z from u_z was dropped for convenience.

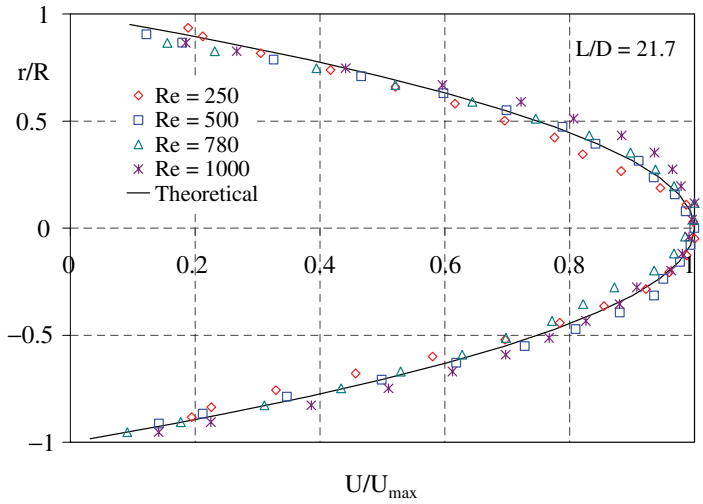

Figure 3. Velocity profiles at the various Reynolds numbers considered in this study.

2.2 Data Processing & Analysis

To analyze the flowfield with periodic forcing, it is useful to consider the axial velocities $\tilde{u}(\mathbf{x},t)$ decomposed according to the so-called triple decomposition (Hussain and Reynolds, 1970; Reynolds and Hussain, 1972):

$$\tilde{u}(\mathbf{x},t) = U(\mathbf{x}) + u_c(\mathbf{x},t) + u(\mathbf{x},t) \tag{1}$$

Where $U(\mathbf{x})$ is the mean velocity, defined as:

$$U(\mathbf{x}) \equiv \overline{\tilde{u}(\mathbf{x},t)} = \lim_{\tau\to\infty} \frac{1}{\tau} \int_0^{\tau} \tilde{u}(\mathbf{x},t)dt \tag{2}$$

$u_c(\mathbf{x},t)$ is the purely periodic, or coherent component and $u(\mathbf{x},t)$ is the random turbulence. In the present setup, phase-averaged velocity (denoted $\langle\rangle$) was calculated according to:

$$\langle\tilde{u}(\mathbf{x},t)\rangle = \lim_{N\to\infty} \frac{1}{N} \sum_{n=1}^{N} \tilde{u}(\mathbf{x},t+nT) \tag{3}$$

where T is the forcing period $1/f$ and

$$u_c(\mathbf{x},t) = \langle\tilde{u}(\mathbf{x},t)\rangle - U(\mathbf{x}) \tag{4}$$

and thus

$$\tilde{u}(\mathbf{x},t) = \langle\tilde{u}(\mathbf{x},t)\rangle + u(\mathbf{x},t) \tag{5}$$

Finally, we define the total unsteady component as the sum of the coherent and turbulent components, thus:

$$u_T(\mathbf{x},t) = u_c(\mathbf{x},t) + u(\mathbf{x},t) \tag{6}$$

In periodically forced flows, for example a forced turbulent free shear layer (Oster *et al.,* 1978), this description is particularly apt as large periodic coherent structures transfer momentum across the shear layer while smaller scale apparently non-coherent turbulence produce small scale mixing. Because the larger scales produce large-scale shear, they also dictate the behavior of the turbulence at the small scales. The power spectral density (PSD) of the resulting non-coherent turbulence was also investigated

in an attempt to confirm the existence of turbulence using the "– 5/3 law" (Kolmogorov, 1941; Grant *et al.,* 1961). Fig. 4 illustrates the triple decomposition and is based on a hot-wire trace at the pipe centerline several diameters downstream of the actuator.

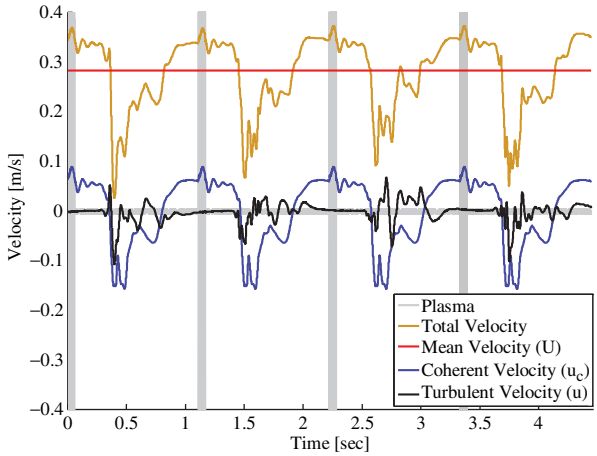

Figure 4. Hot-wire traces, illustrating the triple decomposition. Plasma pulses are shown in grey.

The traces illustrate the total velocity $\tilde{u}$ (orange) decomposed into the mean, coherent and turbulent components (red, purple and black, respectively; see equation 1). The plasma pulse-width, when the actuator is active, is shown in grey. Strictly speaking the "turbulent" component should be considered to be a "non-coherent" component until proven that it is in fact turbulence. This is assumed in the discussion below, but considered in more detail in section 3.5. Preliminary data acquired at different locations in the pipe showed that pulsing the actuators resulted in greater levels of turbulence than if the actuators were run continuously at 100% duty cycle (*DC*). This has the advantageous effect of producing larger turbulent energy at a lower input power because input power is directly proportional to *DC*. Henceforth the vast majority of data was acquired with pulsing.

In this investigation we wish to maximize dependent parameters, such as streamwise turbulence u' ($'$ indicates the rms value), that depend on the following dimensional parameters:

$$u' = u'(r,D,L,\mu,\rho,f,U,T_{on},F_p,C_i) \tag{7}$$

From dimensional analysis, we can show that:

$$u'/U = \varphi(Re,L/D,\xi,f^+,C_\mu,DC,C_i) \tag{8}$$

where $\xi = 2r/D$, $f^+ = fD/U_b$ is the forcing Strouhal number, $C_\mu = F_p \,/\, {}^1\!/_2\, \rho U_b^2 A$ is the time-mean momentum coefficient, $A = \pi D^2/4$ and $DC = T_{on}/T$ is the duty cycle, i.e. fraction of period that the actuator is active. Finally, C_i (i = 1,2,3) refers to the actuator configuration, namely AU, AD and S.

3. DISCUSSION OF RESULTS

3.1. The Optimal Configuration

The first part of this investigation was geared toward determining which actuator produced the highest turbulence level for a given power or momentum input. In order to compare the effectiveness of the three configurations, measurements of centerline and near-wall velocity were acquired for different forcing Strouhal and Reynolds numbers for each configuration. Sample data for the coherent component at the centerline and near the wall are shown in figs. 5 and 6 below.

Fig. 5 shows the basic differences between the actuators as regards their effect on the flow at the pipe centerline (note that the data is vertically shifted for clarity). Beginning with the lower two curves, (axisymmetric-upstream – AU) and (axisymmetric-downstream – AD), it is seen that the plasma pulse produces a Helmholtz resonance in the plenum. This was confirmed by increasing the pipe length and observing a direct correlation with the Helmholtz frequency. The resonance phenomenon was considered to be outside of the scope of this investigation and hence not investigated further. Of importance here is the disturbance advected from upstream, whose effect is seen starting at t/T~0.22. Due to the time taken

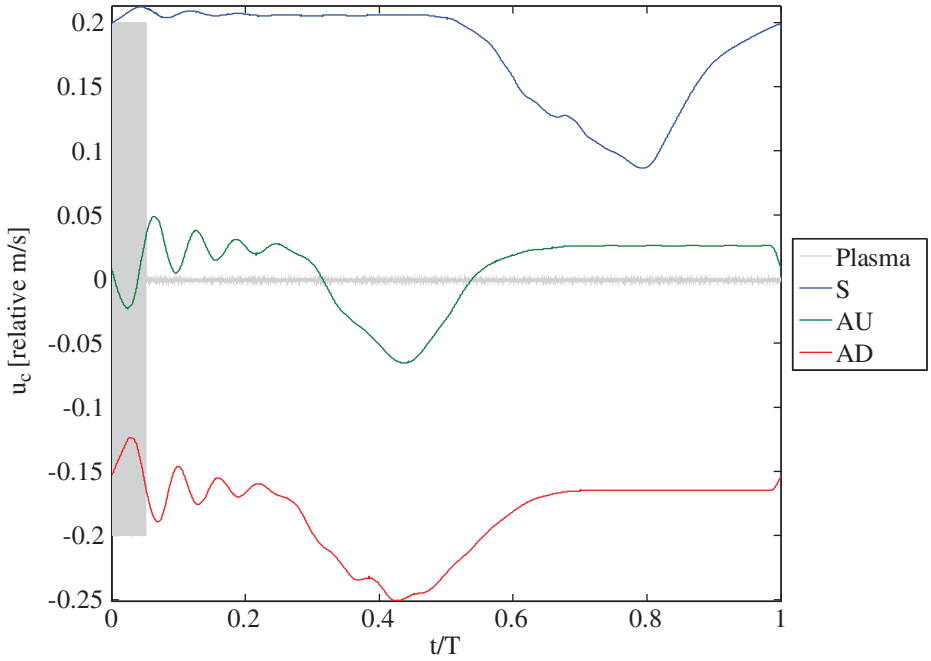

Figure 5. Coherent velocity component at the pipe centerline (ξ = 0) for *Re* = 500 and *L/D* = 5.9 downstream of the different actuators, illustrating the effect of actuator configuration. Forcing is at f^+ = 0.064, *DC* = 5% and C_μ = 1.4. u_c is shifted on the axis for clarity.

for the disturbance to be advected from the upstream actuator location, these disturbances appear "later" as a decrease in the centerline velocity. The resonance associated with the Swirl actuator is much smaller because it does not directly force the oscillation. However, the reduction in centerline velocity and the duration of this reduction are noticeably larger than those of the axisymmetric actuators. The net result is that the measured rms coherent disturbance associated with the S configuration is approximately 40% larger than the AU actuator and 20% larger than the AD actuator. In fact, the rms values of the swirl configuration are larger over virtually the entire Strouhal number range considered here (see fig. 7 below). Similar observations were made in the near wall region and these are shown in fig. 6. Here the principal contribution of the axisymmetric actuators is the Helmholtz resonance and the coherent

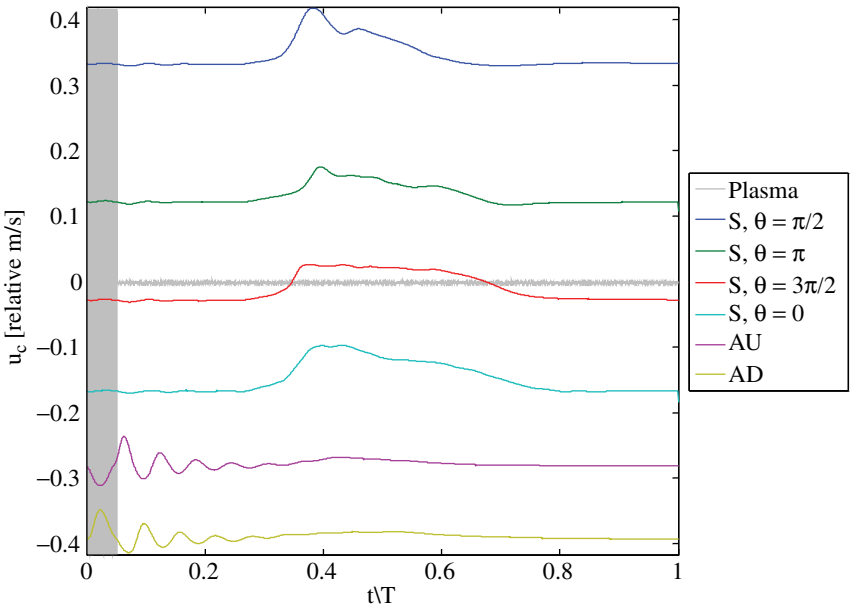

Figure 6. Coherent velocity component at ξ=0.92 for *Re* = 500 and *L/D* = 5.9 downstream of the different actuators, illustrating the effect of actuator configuration. Forcing is at f^+ = 0.064, *DC* = 5% and C_μ = 1.4.

disturbance is almost negligible. Similar observations were made with respect to turbulence measurements. The corresponding rms of the total unsteady component u'_T is shown for a range of reduced frequencies in fig. 7. Apart from data at $f^+ > 0.3$, the swirl actuator consistently produces larger overall perturbations.

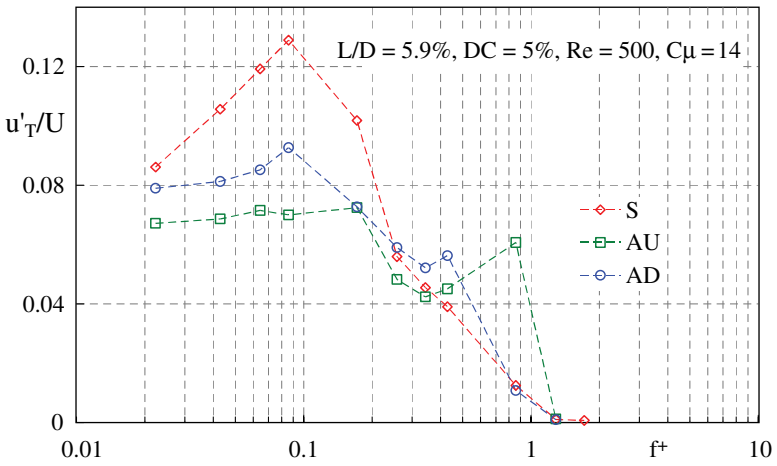

Figure 7. Rms of the total unsteady (coherent plus turbulent velocity) components at ξ=0.92 for *Re* = 500 and *L/D* = 5.9 downstream of the different actuators, illustrating the effect of actuator configuration.

3.2. Effect of Frequency

Based on the data shown above, all further experimentation was conducted using the swirl configuration. Initially, low duty cycles were selected principally because power consumption increases linearly with the *DC*. The effect of frequency at constant power (or *DC)* is shown for the centerline velocity in fig. 8 for *L/D* = 5.9 and *Re* = 500. Data are shown for increasing frequency, starting at f = 0.15Hz (f^+ = 0.013) and increasing to f = 4Hz (f^+ = 0.344). A comparison of the graphs shows a number of different features. The lower frequencies (or larger periods *T)* produce longer plasma pulse-widths, because $T_{on} = DC \times T$ and hence the effect of a single pulse is larger. For example, by comparing f = 0.15Hz with f = 0.88Hz it can be seen that the disturbance has a longer duration, approximately twice as large. However, at low frequencies there is a relatively long laminar component and hence the "intermittency" is rather low even though the disturbance duration is large. Clearly, these counteracting effects do not produce the largest coherent or turbulent component. In fact, at f = 0.15Hz, the laminar duration is approximately four times larger than the disturbed duration. Increasing the frequency simultaneously reduces the duration of the disturbances but also reduces the duration that the flow is laminar and hence increases the intermittency. Further increases in frequency, for example from f = 0.88Hz to f = 1.10Hz showed two effects. Firstly, the laminar component is further diminished and secondly the amplitude of the disturbance decreased. It is clear that the optimum in the coherent disturbance lies in this range. Indeed, as will be shown below in fig. 8, the optimum is f^+~0.08 which corresponds to f^+~1Hz. With further increases in frequency the disturbance amplitude decreases although it is difficult to ascertain qualitatively from these figures how the purely turbulent component is affected (this is discussed below). It is evident, however, that the successively shorter T_{on} associated with the higher frequencies has a diminishing effect on the flow.

Summaries of coherent and turbulent rms components are shown in figs. 9a and 9b respectively. As expected from the above discussion, the peak coherent contribution occurs at f^+~0.08 (fig. 9a). The effect appears to saturate with very little effect on the coherent component for $C_\mu > 1.4$. Note, however, that as the Reynolds number increases the oscillatory coherent component decreases. This is not a Reynolds number effect but occurs because the relative momentum produced by the actuator, namely C_μ, decreases. Similar trends are also seen with respect to the purely turbulent component shown in fig. 9b. These observations are best understood in the context of previous work conducted in rotating (swirling) flows. When flows with an axial component are subjected to a swirling component the flows can exhibit axial flow reversal. The phenomenon is called "vortex breakdown" and is generally accompanied by high levels of turbulence. In a theoretical study, Squire (1960) considered three idealized swirling flows and determined that breakdown occurs when the maximum swirling velocity is 1.0 to 1.2 times larger than the axial velocity. Harvey (1962) showed that the change from one regime to another is reversible, and is

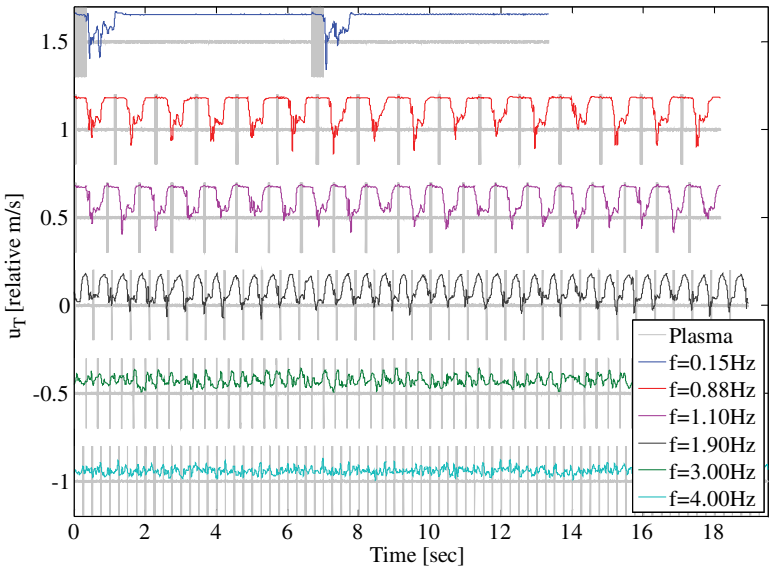

Figure 8. Hot-wire velocity signals at the pipe centerline (ξ=0) for Re = 500 and L/D = 5.9 showing increasing pulse frequency with *DC* = 5% and C_μ = 3.6.

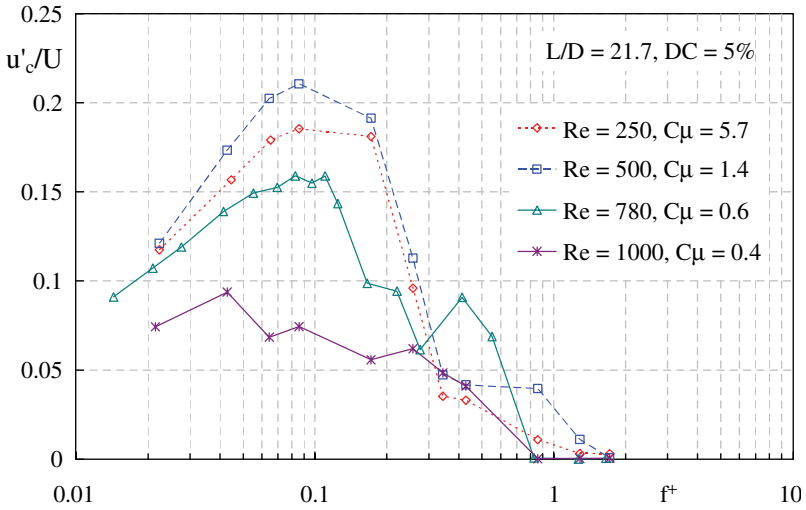

Figure 9a. Rms of the coherent velocity component at ξ=0 for a range of reduced frequencies and Reynolds numbers.

characteristic of a 'critical' phenomenon and not an instability-related one. In the present experiments, the swirling flow is more complex and the ratio of peak swirling velocity to axial velocity is not a reliably parameter. A more meaningful parameter is the swirl number (Gupta *et al.,* 1984), which is the ratio of the axial flux of angular momentum G_θ to the axial flux of axial momentum G_z, normalized by the radius, namely:

$$S_{\theta z} = \frac{G_\theta}{RG_z} = \frac{\int_0^R u_z v_\theta r^2 dr}{R\int_0^R u_z^2 r dr} \tag{9}$$

It can reasonably be assumed that there is some proportionality between the swirl number and the ratio of the swirling momentum to the axial momentum, namely C_μ (in the next section it is shown that $S_{\theta z} \propto C_\mu^{1/2}$). Therefore, when C_μ exceeds a critical value and the vortex breaks down, typically C_μ~O(1), further increases in momentum input will have very little effect on the flow. When C_μ is

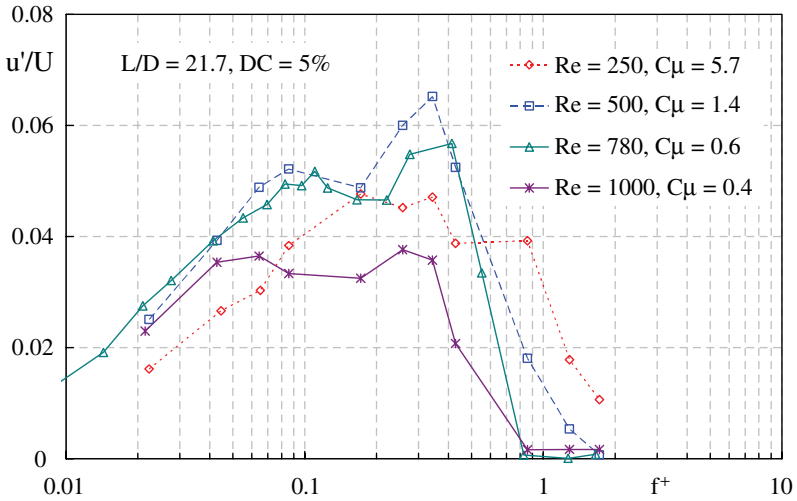

Figure 9b. Rms of the turbulent velocity component at $\xi = 0$ for a range of reduced frequencies and Reynolds numbers.

below the critical value and breakdown does not occur, a reduction in the momentum input will have a progressively smaller effect on the flow. This explanation is fully consistent with the observations made in figs. 8 and 9.

It is noted further that the generation of purely incoherent turbulence (fig. 9) has a somewhat different trend to that of the coherent component. Clearly at the low frequencies the laminar component is so large that the overall rms turbulence level is low. With increasing frequency, the turbulence reaches a plateau but shows a distinct peak at approximately f^+~0.34. This peak was elucidated by means of flow visualization described below. As the frequency increases further, the turbulence level drops further because the decreasing pulse-widths have a diminishing effect on the flow; similar effects were observed with regard to the coherent component above.

3.3. Effect of Pulse Width

In previous research with DBD actuators, where pulsed actuation was involved, pulse width T_{on} is always non-dimensionalized with respect to the pulsation frequency (or period), namely the duty cycle DC. This is convenient when performing parametric studies because the power input is directly proportional to DC. For the present experiments, this approach was also considered but there was a significant lack of correlation of the data (see fig. 10). In light of this a different scaling parameter was sought. It was ascertained that the data scaled better with the pulse-width T_{on} and hence the scaling was believed to be related to the viscous time scale R^2/ν. This was not fully verified in the present investigation because the pipe diameter was not varied. However the basis for this scaling can be understood by considering the problem of spin-up of an axisymmetric fluid.

Consider the Navier-Stokes equations in cylindrical coordinates for a pipe flow that is fully developed in the axial (z) direction. If the pipe wall is suddenly set in rotational motion ΩR at $t = 0$, then the rotational swirling fluid velocity can be found from the equation of motion in the azimuthal direction as:

$$\frac{v_\theta}{\Omega R} = \xi + 2\sum_{n=1}^{\infty} \frac{J_1(\lambda_n \xi)}{\lambda_n J_0(\lambda_n)} \exp\left(-\frac{\lambda_n}{\alpha_R}\right) \tag{10}$$

where $\alpha_R = R^2/\nu t$ is the Womersley number ($\nu = \mu/\rho$), J_i are the Bessel functions of the first kind, first and second order $i = (0,1)$ and λ_n are the zeros of the indicial equation $J_1(\alpha_n) = 0$ (see Wedemeyer, 1964). In the present experiments, the "spinning" boundary condition (ΩR) is approximated by the plasma wall jet because when the plasma is initiated, there is a region of high-speed swirl near the wall and a quiescent core flow in the central region. The flow spins-up as time progresses providing that the actuator is operational. To illustrate this, consider the data of fig. 10, where time is scaled with the inverse Womersley number, namely $1/\alpha_R = \nu t / R^2$ in fig. 11. The data correlate more closely with this

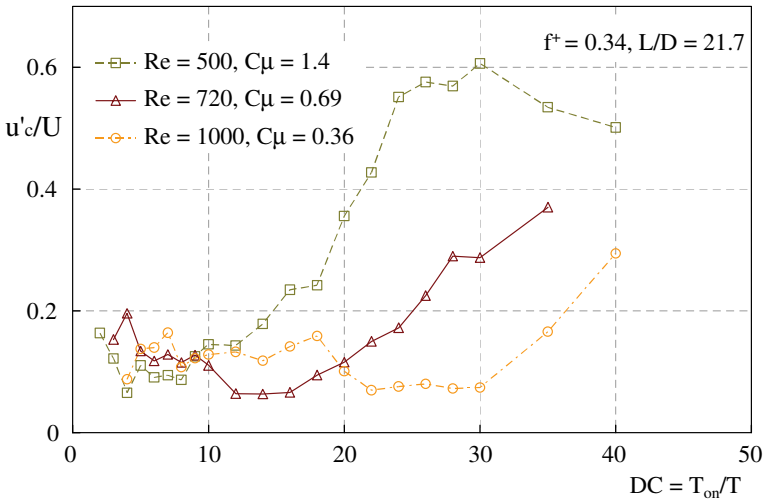

Figure 10. Rms of the coherent velocity component as a function of duty cycle at ξ = 0 for a range of and Reynolds numbers and momentum coefficients.

scaling. Nevertheless, it is seen that in each case the coherent component begins increasing beyond some critical value of vt/R^2 where this critical value decreases with increasing C_μ (indicated in the figure). Furthermore, it is also seen that for $C_\mu = 1.4$ the effect on the coherent velocity component saturates at $vt/R^2 \approx 0.06$. This observation, combined with the large coherent content indicate that vortex breakdown has been attained.

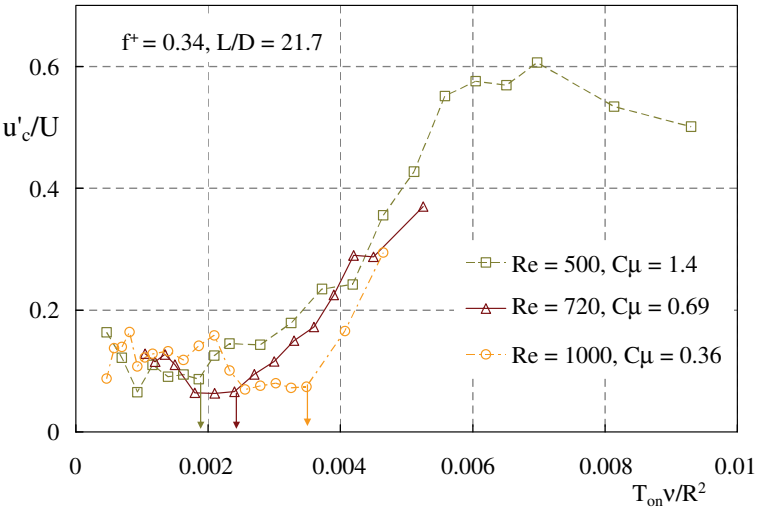

Figure 11. Rms of the coherent velocity component as a function of $1/\alpha_R$ at ξ = 0 for a range of Reynolds numbers and momentum coefficients.

The above discussion can be better understood by assuming a fully developed pipe flow and then substituting equation 10 into equation 9, yielding:

$$S_{\theta z} = \left(4.5\frac{R}{h}C_\mu\right)^{1/2}\int_0^1 (\xi^2-1)\left\{\frac{v_\theta}{\Omega R}(\xi)\right\}\xi^2 d\xi \qquad (11)$$

where equation 11 is integrated numerically. Here we account for the different momentum coefficients employed by assuming a constant characteristic plasma "wall jet-width" h resulting in $C_\mu = (2h/R)(\Omega R/U_b)^2$. Results for the integrated swirl number from equation 11 versus vt/R^2 are

shown in fig. 12 and correspond to the C_μ values in fig. 11. We assert here that when the swirl number reaches a critical value, it begins to have an effect on the vortex development. Here this "critical" value is taken as $S_{\theta z} = 0.12$ for illustrative purposes. The lower line drawn at $S_{\theta z} = 0.12$ through computed values corresponds approximately to the vt/R^2 values indicated in fig. 11. This provides strong support for the notion that the temporal flow behavior is determined by the viscous time scale R^2/v. The upper horizontal line is drawn to correspond to the computed $C_\mu = 1.4$ case at $vt/R^2 = 0.06$ (cf. fig. 11). This can be considered indicative of the swirl number at which the vortex breaks down. It is encouraging to note that this relatively simple analysis indicated a swirl number ($S_{\theta z} = 0.37$) that is of the same order as those observed during observed vortex breakdown in other investigations. Indeed, the theoretical analysis can also provide an assessment of the required vt/R^2 to breakdown for the lower and higher C_μ values. Clearly, if C_μ is too low to produce sufficient swirl, then the breakdown will not occur for all vt/R^2.

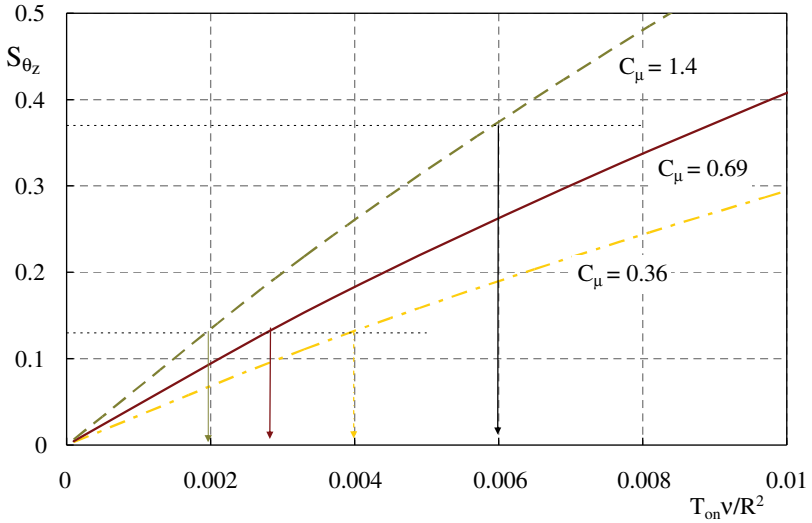

Figure 12. The variation of the Swirl number as a function of inverted Womersley number for different momentum coefficients (cf. fig. 11).

3.4. Flow Visualization

In order to better understand the mechanisms involved with control, smoke was introduced upstream of the entrance contraction via a thin tube. A high-speed (1200 fps) movie of the pipe section containing the actuator was then filmed for several Strouhal numbers. Representative frames of the motion for $f^+ = 0.34$ are presented in fig. 13 at $Re = 500$; at this f^+ the turbulence created was at a maximum and thus this condition was scrutinized further. In these frames the actuator is located at the top of the pipe aligned axially and the field of view is the actuated region. With a duty cycle of 5%, actuation is initiated at $t/T = 0$ (first frame in the sequence) and in the next frame at $t/T = 0.05$ it is terminated. During this time period the smoke filament is seen to move upwards as a result of the introduced swirl due to the fact that it was not aligned precisely on the centerline. The filament swirls around the pipe and by approximately t/T ~0.14 it begins breaking apart and diffusing. New laminar fluid flowing into the field of view (from the right) was not subjected to swirl and the two different flow regimes are clearly identifiable, for example at $t/T = 0.467$. The un-swirled flow progresses further into the pipe and seems to form a jet that moves in a downward direction as it progresses into the pipe. This is indicated by the red line in fig 12. Simultaneously, a smoke filament oriented at approximately –45° can be seen to be moving upstream and this is indicated by the blue line. The reverse flow suggests that a phenomenon resembling local vortex breakdown is taking place, in a periodic manner. Strangely, this is only visible after the actuation has been terminated. It appears that vortex breakdown does not occur immediately after actuation, but there is a time-lag associated with the spin-up process. It is believed that a theory based on the above discussion relating to equations 9 and 10 could provide a basic explanation for the observed effects.

Figure 13. Smoke filament flow visualization at $f^+ = 0.34$, filmed at 1200fps photography.

The present flow visualization sequence also helps explain why this is the frequency at which turbulence has a maximum. Observing the downstream end of the pipe it is clear that the flow exiting the region of the actuator never reverts to a laminar state. That is because the laminar flow entering the actuated region in a Lagrangian sense is subjected to the swirling body force just prior to it exiting the actuated region. This further elucidates the data in fig. 9 where this case corresponds to f = 4Hz.

Thus even though the actuator is operating for 5% of the time, it is producing turbulence continuously downstream of the actuated region. With these considerations we can construct the correct dimensionless group as follows. Firstly, the average time taken for the fluid particles to traverse the pipe is l/U_b where l is the actuator length πD; secondly, time scale for a full actuation cycle is $1/f$; their ratio is the Strouhal number fl/U_b or πf^+. It therefore comes as no surprise that the optimum perturbation frequency is $\pi f^+ \approx 1$. Future work must consider varying the parameter fl/U_b with the concomitant parameter l/D.

3.5. Nature of the Turbulent Flow

In the previous section, the non-coherent flow component was simply termed "turbulent" without offering any substantial evidence of turbulent versus non-coherent flow. To further examine this, two approaches were followed. One was to acquire data arranged in a matrix to determine the nature of phase-averaged profiles; the second was to consider the spectra of the non-coherent component of the flow.

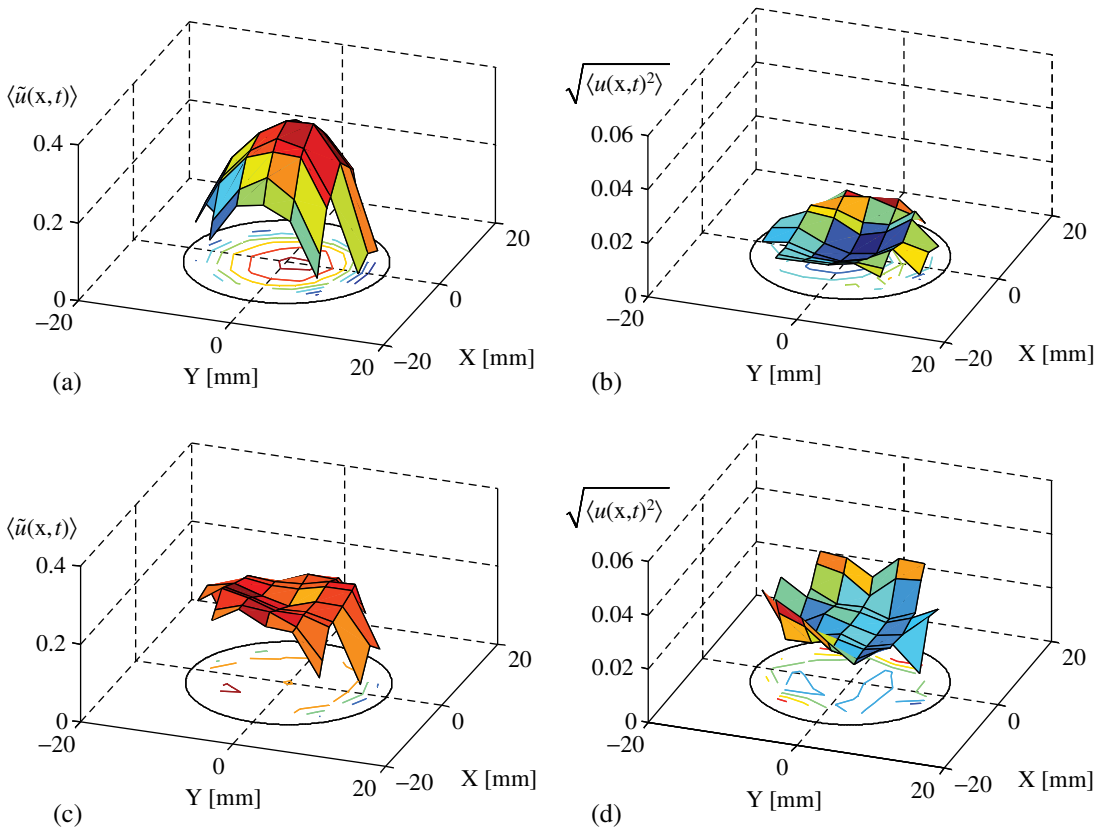

Figure 14. Selected phase-averaged velocity and turbulence within the pipe at L/D = 5.9, Re = 500 and f^+ = 0.08: (a,b) data at t/T = 0; (c,d) data at t/T = 0.57.

Phase-averaged velocity data $\langle \tilde{u}(x,t) \rangle$ and phase-averaged turbulence $\sqrt{\langle u(x,t)^2 \rangle}$ are shown in fig. 14 for selected phases in the left and right hand columns respectively; Re = 500, f^+ = 0.08 and L/D = 5.9. At t/T = 0, the actuation is initiated, but the effects at 5.9 diameters downstream are not yet felt. The level of non-coherence is negligible as this is a laminar flow. As the perturbed flow is washed downstream the centerline velocity drops while the velocity near the wall increases. This was discussed above with respects to figs. 5 and 6. Despite some asymmetry of the flow, due to the asymmetry of the actuator configuration, the phase-averaged profile has a decidedly turbulent form with small changes

over most of the central region of the pipe and steep gradients near the wall. In addition, the turbulence levels are higher near the wall than in the core region. Both of these attributes can be considered typical of turbulent pipe-flow profiles.

The second approach was to assess the data within the framework of Kolmogorov's well-known law:

$$E(k) = C\varepsilon^{2/3}k^{-5/3}$$

where the Taylor's "frozen-turbulence" approximation is assumed, namely that turbulence in a time series is reflective of the variability in space, i.e., fluctuations are not affected by the mean flow, but merely advected and hence

$$E \sim f^{-5/3}$$

For full turbulent flow, this law is valid in inertial sub-range where the scales are smaller than the energy-containing eddies but larger than the viscous ones.

To generate the PSD, the non-coherent components of the velocity signals were low-pass filtered at 150Hz and acquired at 195kHz. The data in each cycle were interpolated to the nearest power of 2, transformed using an FFT algorithm and repeated runs were then averaged. Figs 14a and 14b show PSD data with a factor of 4 difference in the forcing Strouhal number. Although the details of the spectra are different, it can be argued that both have turbulence-like spectra. The spectrum of the lower forcing frequency ($f^+ = 0.08$), which contains a laminar component has "typical" spectrum where the slope increases with increasing frequency. At the higher frequency ($f^+ = 0.34$) there is also a clear –5/3 component, but the slope increases with increasing frequency and this is atypical. It is not clear to the authors why the slope increases.

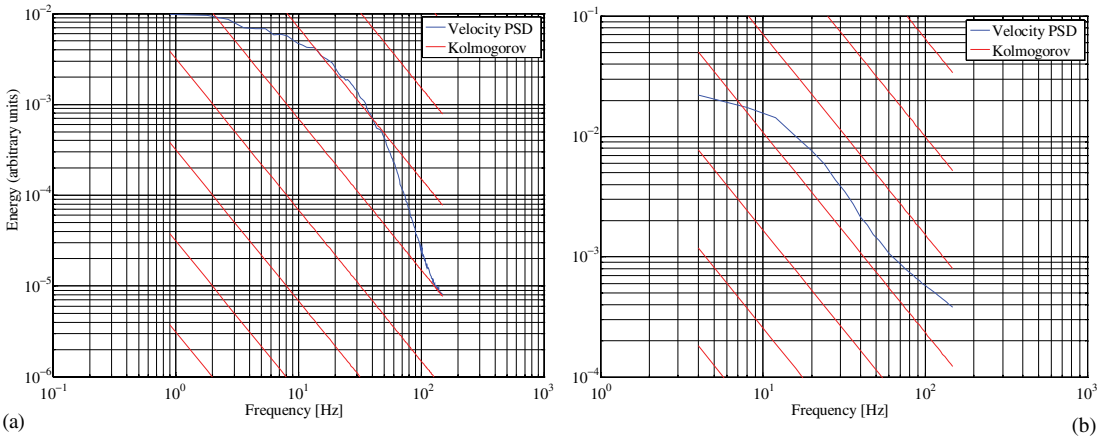

Figure 15. PSD data for relatively low and high frequency forcing for Re = 500 and L/D = 5.9: (a) $f^+ = 0.08$; (b) $f^+ = 0.34$. Only the non-coherent component is considered.

As mentioned in the introduction, because the Reynolds numbers are sub-critical, the coherent and turbulent components will ultimately decay. To illustrate this, measurements at different downstream locations are shown in figs. 16a and 16b. Up to approximately 22 diameters downstream the dependence of both the coherent and turbulent components is similar. For the coherent components (fig. 16a) the optimum frequency appears to become smaller. This may be because the lower frequency perturbations decay more slowly in the downstream direction. Even though the peak coherent component is generated at around $f^+ \sim 0.08$ near the actuator, at approximately 22 diameters downstream the optimum is closer to $f^+ = 0.05$. A similar observation can be made with respect to the turbulence; peak values are around $f^+ = 0.3$ to 0.4 near the actuator, but this peak all but disappears at 22 diameters downstream.

4. MAIN CONCLUSIONS

The main conclusions of this work are listed below:

1. For a given power or momentum input, a pulsed-swirl actuation produces greater rms levels of coherent and turbulent oscillations than pulsed axi-symmetric actuation.
2. The largest coherent oscillations occur at a reduced frequency of approximately 0.08 while peak non-coherent disturbances occur around 0.34.

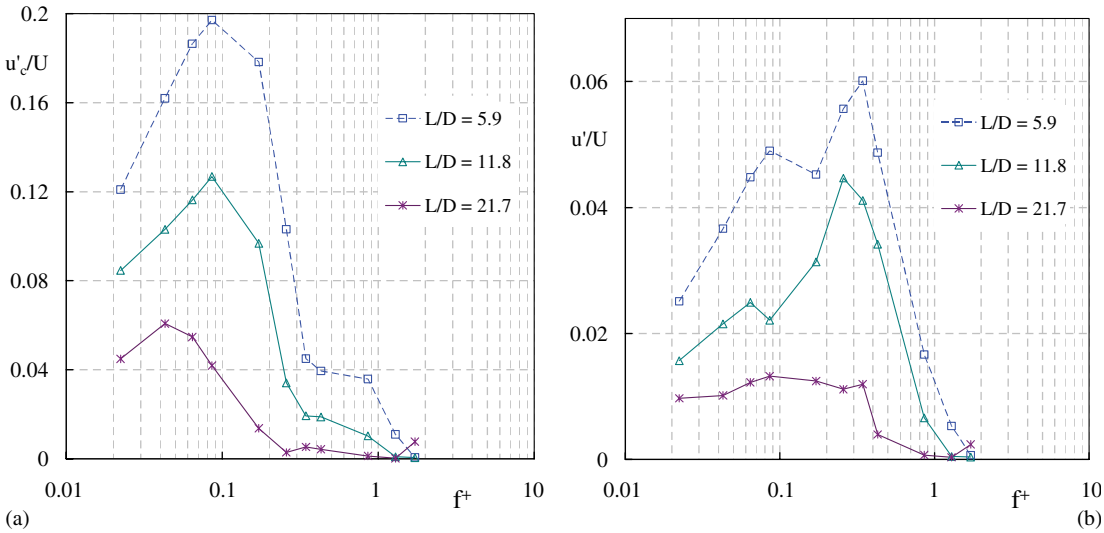

Figure 16. Decay of (a) coherent and (n) non-coherent disturbances, *Re* = 500, C_μ = 1.4.

3. The commonly used duty cycle was limited in its suitability for explaining the flow mechanisms. Based on preliminary data and a simple analytical model, a more appropriate pulse-width parameter must be scaled with viscosity and pipe radius.
4. The length of the swirl actuator, non-dimensionalized with respect to frequency and mean flow velocity is the main parameter for controlling the purely turbulent component of the flow.
5. High-speed flow visualization indicated a complex three-dimensional flow structure within the actuated flow regime, with regions of localized reverse flow indicating vortex breakdown.
6. Based on mean flow profiles and turbulent spectra it was concluded that the non-coherent flow component had much in common with turbulence.

REFERENCES

1. Carmichael B.H., "Low Reynolds number airfoil survey," 1981, Vol. 1. NASA CR 165803.
2. Corke, T., Post, M. and Orlov, D., "Single dielectric barrier discharge plasma enhanced aerodynamics: physics, modeling and applications", 2009, Springer, *Experiments in Fluids*, Volume 46, Number 1, pp. 1–26.
3. Eckhardt, B., Schneider, T. M., Hof, B., and Westerweel, J., "Turbulence Transition in Pipe Flow," 2007, *Annu. Rev. Fluid Mech.*. 39:447–68.
4. Eliahou, S., Tumin, A. and Wygnanski, I., "Laminar-turbulent transition in Poiseuille pipe flow subjected to periodic perturbation emanating from the wall," 1998b, *J. Fluid Mech.* 361, 333–349.
5. Enloe C, McLaughlin T E, VanDyken R D, Kachner K D, Jumper E J and Corke T C, "Mechanisms and responses of a single dielectric barrier plasma actuator: plasma morphology", 2004, *AIAA J.* 42 589–94.
6. Fox, J. A., Lessen, M. and Bhat, W. V., "Experimental investigation of the stability of Hagen-Poiseuille flow," 1968, *Phys. Fluids* 11, 1–4.
7. Goldstein, S. "A note on roughness," 1936, *Aero. Res. Counc.* R&M 1763.
8. Grant, H. L., Stewart R. W. and Moilliet, A. "Turbulence spectra from a tidal channel," 1961, *J. Fluid Mech.*, 12, 241–263.
9. Greenblatt D., Göksel B., Schüle C.Y., Paschereit C.O., "Dielectric barrier discharge flow control at very low flight Reynolds numbers, " 2008, *AIAA Journal*, vol. 46, Issue 6, pp. 1528–1541.
10. Gupta, A. K., Lilley, D. G. and Syred, N., *Swirl Flows*, Abacus press, Cambridge, 1984.
11. Han, G., Tumin, A. and Wygnanski, I., "Laminar-turbulent transition in Poiseuille pipe flow subjected to periodic perturbation emanating from the wall. Part 2. Late stage of transition," *J. Fluid Mech.*, 2000, Vol. 419, pp. 1–27.
12. Harvey, J. K., "Some observations of the vortex breakdown phenomenon," *Journal of Fluid Mechanics*, Vol. 14, pp. 585–592.

13. Hussain, A.K.M.F. and Reynolds, W.C., "The Mechanics of an Organized Wave in Turbulent Shear Flow", *J. Fluid Mechanics*, 1970, Vol. 41, part 2, pp. 241–258.
14. Kerswell R.R. "Recent progress in understanding the transition to turbulence in a pipe," 2005, *Nonlinearity* Vol. 18, R17–44.
15. Kolmogorov, A. N., "The local structure of turbulence in incompressible viscous fluids at very large Reynolds numbers," 1941, Dokl. Akad. Nauk. SSSR, 30, 301-305. Reprinted in 1991: *Proc. R. Soc. Lond. A*, 434, 9–13.
16. Leite, R. J. "An experimental investigation of the stability of Poiseuille flow," 1959, *J. Fluid Mech.* 5, pp. 81–97.
17. Moreau, E., "Airflow control by non-thermal plasma actuators", 2007, *J. Physics -London-D Applied Physics*, Vol. 40; No. 3, pp. 605–636.
18. Morkovin, M. V. and Reshotko, E., "Dialogue on progress and issues in stability and transition research," 1990, In *Laminar-Turbulent Transition*, IUTAM Symp. Toulouse (ed. D. Arnal & R. Michel), pp. 1–29. Springer.
19. Oster D., Wygnanski I., Dziomba B. and Fiedler H., "The effects of initial conditions on the two-dimensional mixing layer", 1978, In: Fiedler H , ed. *Structure and Mechanisms of Turbulence I*. Berlin: Springer-Verlag.
20. Post, M.L. Corke, T. C., "Separation Control on High Angle of Attack Airfoil Using Plasma Actuators", 2004, *AIAA Journal*, Vol. 42, No. 11, pp. 2177–2184.
21. Reshotko, E., "Experimental study of the stability of pipe flow. I. Establishment of an axially symmetric Poiseuille flow," 1958, *Jet Propulsion Laboratory*, Progress Rep. 20-364. Pasadena, California.
22. Reshotko, E. Tumin, A., "Role of Transient Growth in Roughness-Induced Transition", 2004, *AIAA Journal*, Vol. 42, Part 4, pp. 766–770.
23. Reuter J. and Rempfer D., "Analysis of pipe flow transition. Part II. Energy transfer", 2005, *Theoret. Comput. Fluid Dynamics*, 19: 39–64.
24. Reynolds, O., "An Experimental Investigation of the Circumstances Which Determine Whether the Motion of Water Shall Be Direct or Sinuous, and of the Law of Resistance in Parallel Channels", 1883, *Philosophical Transactions of the Royal Society of London*, Vol. 174, pp. 935–982.
25. Reynolds, W.C and Hussain, A.K.M.F., "The Mechanics of an organized Wave in Turbulent Shear Flow. Part 3. Theoretical models and comparisons with experiments", *J. Fluid Mechanics*, 1972, Vol. 54, part 2, pp. 263–288.
26. Roth J., Sherman D. and Wilkinson S., "Boundary layer flow control with one atmosphere uniform glow discharge surface plasma," AIAA Paper 1998-0328, 1998.
27. Schlichting, H. and Gersten, K., "Boundary Layer Theory," McGraw-Hill Book Co., New York, USA, 1999.
28. Schubauer, G.B. and Skramstad, H.K., "Laminar-Boundary-Layer Oscillations and Transition on a Flat Plate", 1943-48, National Bureau of Standards Research Paper 1772.
29. Squire, H.B., "Analysis of the vortex breakdown phenomenon, part I," Report No. 102, 1960, Aeronautics Department, Imperial College, London.
30. Wedemeyer, E.H., "The unsteady flow within a spinning cylinder," *J. Fluid Mech.*, 1964, vol. 20, part 3, pp. 383–399.
31. Wieselsberger, C., "Der Luftwiderstand von Kugeln," 1914, ZFM. 5 pp. 140–144.